Icarus 410 (2024) 115892

Contents lists available at ScienceDirect

Icarus

journal homepage: www.elsevier.com/locate/icarus

First magnetic and spectroscopic constraints on attenuated space weathering at the Chang'e-5 landing site

Yuqi Qian [a,b], Long Xiao [a,l,*], Jiawei Zhao [a], James W. Head [c], Qi He [a], Huiru Xu [d], Feizhou Wang [e], Xiaoping Zhang [f], Xianquan Ping [a], Wen Zeng [g], Xing Wang [h], Joseph Michalski [b], Jiacheng Liu [b], Binlong Ye [b], Meizhu Wang [i], Lingzhi Sun [j], Yong Pang [k], Jiang Wang [a], Siyuan Zhao [a]

[a] State Key Laboratory of Geological Processes and Mineral Resources and School of Earth Sciences, China University of Geosciences, Wuhan, China
[b] Department of Earth Sciences and Laboratory for Space Research, The University of Hong Kong, Hong Kong, China
[c] Department of Earth, Environmental and Planetary Sciences, Brown University, Providence, RI, USA
[d] School of Geophysics and Geomatics, China University of Geosciences, Wuhan, China
[e] Analytical and Testing Center, Wuhan University of Science and Technology, Wuhan, China
[f] State Key Laboratory of Lunar and Planetary Sciences, Macau University of Science and Technology, Macau, China
[g] Badong National Observation and Research Station of Geohazards, China University of Geosciences, Wuhan, China
[h] Key Laboratory of Lunar and Deep Space Exploration, National Astronomical Observatories, Chinese Academy of Sciences, Beijing, China
[i] Key Laboratory of Space Active Opto-Electronics Technology, Shanghai Institute of Technical Physics, Chinese Academy of Sciences, Shanghai, China
[j] Department of Earth Sciences, Hawaii Institute of Geophysics and Planetology, University of Hawaii at Manoa, Honolulu, HI, USA
[k] Beijing Spacecrafts, Beijing, China
[l] Center for Excellence in Comparative Planetology, Chinese Academy of Sciences, Hefei, China

ARTICLE INFO

Keywords:
Chang'e-5
Space weathering
Vibrating sample magnetometer
Mössbauer spectrometer
Visible near-infrared spectroscopy

ABSTRACT

Space weathering is a primary process altering the lunar surface, producing submicroscopic iron particles embedded in soil grains, which have diagnostic magnetic and spectroscopic effects. However, the space weathering of lunar soils from young geological units remains mysterious without solid constraints from returned samples. Chang'e-5 mission is the first lunar sample-return mission in decades. The Chang'e-5 landing and sampling unit (~2.0 Ga) is much younger than all Apollo and Luna units (>3.0 Ga). It has provided an unprecedented opportunity to reveal the recent space weathering characteristics with both returned soil samples and *in situ* investigation data. In this study, magnetic approaches (Vibrating Sample Magnetometer, Electron Paramagnetic Resonance Spectrometer, Mössbauer Spectrometer) were used to characterize the Chang'e-5 lunar soil for the first time after the return of the samples, strongly supporting it is among the most immature soils on the Moon with a metallic iron abundance of 0.42% and an Is/FeO value of 14^{+6}_{-10}. Additional Landing Camera and Lunar Mineralogical Spectrometer (480–3200 nm) data obtained surrounding the sampling area were used to study the lateral effects of rocket exhaust. All data from soil samples and *in situ* observations have offered magnetic and spectroscopic constraints on the space weathering state of the Chang'e-5 site. The combined effects of rocket exhaust by removing the top highly weathered soil and the young age of the landing site with lesser degree of impact reworking may attenuate the maturity of Chang'e-5 lunar soils.

1. Introduction

Space weathering, induced continuously by solar winds, cosmic rays, and micrometeorites (Hapke, 2001), is a common process occurring on the surface of airless bodies including the Moon. Maturity is an index to characterize the space weathering degree of lunar soil. A variety of indices including mean grain size, agglutinate abundance, solar wind gases abundances (N, C, and trapped rare gases), solar flare track density, and submicroscopic iron (smFe) particles are used to quantify the lunar soil maturity (Morris, 1976). Nowadays, the value of Is/FeO (the

* Corresponding author at State Key Laboratory of Geological Processes and Mineral Resources and School of Earth Sciences, China University of Geosciences, Wuhan, China.
E-mail address: longxiao@cug.edu.cn (L. Xiao).

https://doi.org/10.1016/j.icarus.2023.115892
Received 23 July 2023; Received in revised form 18 November 2023; Accepted 21 November 2023
Available online 24 November 2023

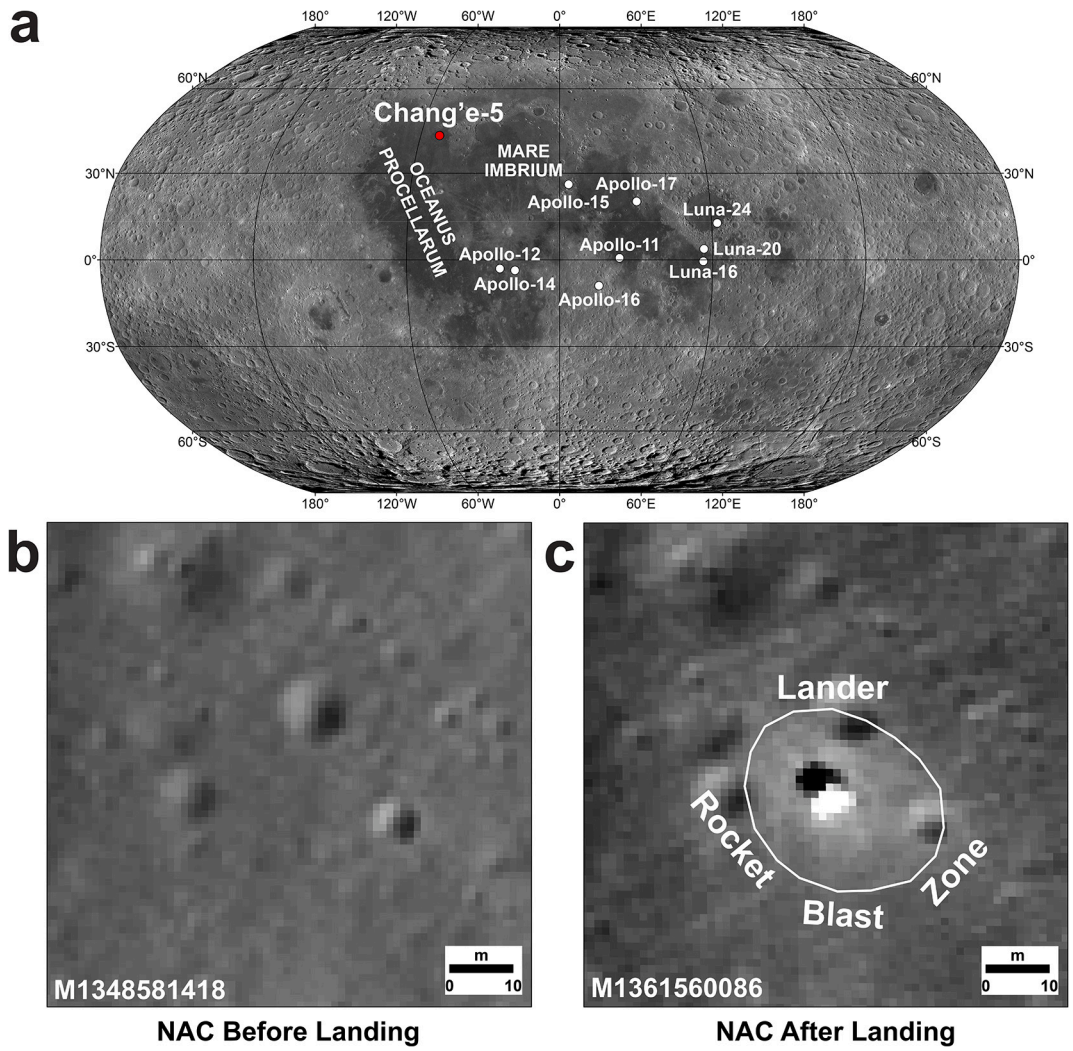

Fig. 1. CE-5 landing site. a. CE-5 landing site in northern Oceanus Procellarum. b. NAC image (M1348581418) of the landing site before landing. c. NAC image (M1361560086) of the landing site after landing. The white polygon indicates the rocket blast zone. These two images have a spatial resolution of ~1 m/pixel. North is up.

intensity of the characteristic ferromagnetic resonance normalized to total iron content) is regarded as the only golden standard of lunar soil maturity because other indices may saturate or be affected by bulk composition (Morris, 1976). It correlates well with smFe particle abundance, which usually occurs on the rims of soil grains and within agglutinates, through micrometeorite vaporization and/or solar wind sputtering and redeposition (Keller and McKay, 1997). Submicroscopic iron particles are composed of metallic (Fe^0), ferrous (Fe^{2+}), and ferric irons (Fe^{3+}) (Guo et al., 2022a; Guo et al., 2022b; Li et al., 2022a; Thompson et al., 2016; Xian et al., 2023). Fe^0 is the dominant phase, which is able to be characterized by spectroscopic and magnetic approaches (Bentley et al., 2011; Morris, 1980).

Submicroscopic metallic iron ($smFe^0$) usually has grain sizes $\leq$2 μm (Pieters and Noble, 2016). It has prominent effects on the visible and near-infrared (VNIR) spectra of lunar soils by reducing the albedo and diminishing the absorption features (Hapke, 2001; Pieters and Noble, 2016). The nanophase iron ($npFe^0$, typically 1–15 nm in diameter) tends to darken and redden the spectra; and the microphase iron ($mpFe^0$, typically ~40 nm-2 μm in diameter) darkens the spectra in all wavelengths (Noble et al., 2007; Pieters and Noble, 2016). Solar wind and micrometeoroid impact are primary processes to form $npFe^0$ and $mpFe^0$, respectively (Morris, 1980). Because of the formation of metallic iron (Fe^0), the space-weathered lunar soils have additional ferromagnetism compared to their original source materials, that can be revealed by magnetic resonance techniques (Bentley et al., 2011; Morris, 1980), such as hysteresis loop and ferromagnetic resonance. In addition, the Mössbauer spectroscopy is sensitive to both the valence state (0, +2, +3) and the local chemical environment of ^{57}Fe (Morris et al., 1998). This provides another efficient method to quantify the space weathering effects, especially when all of the valence states of iron were discovered as space weathering products (Guo et al., 2022a; Guo et al., 2022b; Li et al., 2022a; Thompson et al., 2016; Xian et al., 2023).

Space weathering has been studied extensively since the Apollo era. However, it was only after the Chang'e-3 (CE-3) mission in 2013 and the Chang'e-4 (CE-4) mission in 2019 that the VNIR spectra of the undisturbed surface soils were measured to enable the study of primitive space weathering effects (Gou et al., 2020; Wang et al., 2017). It was not until the Chang'e-5 mission (CE-5) in 2020 that both *in situ* VNIR spectra and soil samples were obtained concurrently. Therefore, the CE-5 mission has offered an unprecedented opportunity to characterize the space weathering effects on lunar soils in their original state and with returned samples by the state-of-art laboratory approaches (Chen et al., 2023).

The CE-5 soils were returned from a mare basaltic plain in northern Oceanus Procellarum (Fig. 1) (Qian et al., 2021b). The CE-5 landing site has an age of 2.0 Ga (Che et al., 2021; Li et al., 2021), at least 1.0 Ga

younger than all previous Apollo and Luna landing sites (>3.0 Ga) (Snape et al., 2016). Space weathering on such a young mare unit was never studied. So far, several studies have discussed the space weathering of the CE-5 soil but cannot reach an agreement on whether it is mature or immature, or can only represent a few soil grains (Guo et al., 2022a, 2022b; Li et al., 2022b; Xian et al., 2023). On the basis of the particle size distribution (finer and better sorted than Apollo soils), Li et al. (2021) proposed the CE-5 soil is mature. Lu et al. (2022) also suggested that the CE-5 soil is mature with $smFe^0$ abundance of >1% based on the *in situ* VNIR data and the Hapke model. In contrast, based on the spectral slope of 950/750 nm and 1600/700 nm from the same data, Wu et al. (2022) proposed that the CE-5 soil is not as mature as previously thought with a $smFe^0$ abundance of 0.14%. In addition, the low agglutinate abundance (~16.6%) of the CE-5 soil (Li et al., 2021) is lower than all Apollo mature soils (>30%) (Graf, 1993), inconsistent with a mature soil. However, all those constraints were based on other indices rather than Is/FeO, the golden standard of lunar maturity state based on magnetic measurements. The question of whether the CE-5 soil is mature or immature remains mysterious. Solving it would shed light on building a complete picture of space weathering on such a young mare unit.

In this study, magnetic approaches were applied first to quantify the maturity of the CE-5 bulk soil. Magnetic techniques were widely used in the analysis of Apollo and Luna lunar soils (Morris, 1980) but for the first time applied to the CE-5 soils. Rocket plume-regolith interactions were analyzed based on the *in situ* Lunar Mineralogical Spectrometer (LMS) and Landing Camera (LCAM) data. In consideration of the ground truth from the magnetic measurements, Hapke radiative transfer modeling of LMS data was further used to estimate the abundance of space weathering products at the landing site. Taken together, these data permit discussing the space weathering on a young mare basalt, cross-validated by *in situ* data and returned soil samples.

2. Materials and methods

2.1. Chang'e-5 lunar samples

CE-5 lunar soil samples CE5C0600, CE5Z0906YJ, and CE5Z0204YJ from the China National Space Administration were used for magnetic measurements in this study (Table 1). CE5C0600 (300 mg) was collected from the surface by a robotic arm (Deng et al., 2021). CE5Z0906YJ (200 mg) and CE5Z0204YJ (150 mg) soils were obtained through drilling (Zheng et al., 2022) from a depth of 0.10 m and 0.65 m, respectively. 8, 4, and 4 basaltic fragments (Fig. S1) with mass varying from 0.10 to 5.18 mg were picked from CE5C0600, CE5Z0906YJ, and CE5Z0204YJ soils for further vibrating sample magnetometer (VSM) and electron paramagnetic resonance (EPR) measurements, in order to better represent the local bedrock.

2.2. Vibrating sample magnetometer

The hysteresis parameters of the CE-5 lunar soil CE5C0600 (6.02 mg), and lithic fragments selected from CE5C0600, CE5Z0906YJ (CE5-0906-01), and CE5Z0204YJ (CE5-0204-01), were obtained by the Lake Shore 8604 VSM with a high sensitivity of magnetization intensity (15 nemu) at Analytical and Testing Center, Wuhan University of Science and Technology (Fig. 2a). The hysteresis loop was measured at room temperature with a maximum field of 1.9 T (field step size of 0.01 T) and averaging time of 0.2 s. Saturation magnetization (M_s), saturation remanent magnetization (M_{rs}), and coercivity (H_c) were calculated with an MATLAB-based open-source software HystLab (Paterson et al., 2018), and remanent coercivity (H_{cr}) was estimated by the Delta M curve (Fig. S2) obtained by another MATLAB-based open-source software HYSITS (Erdyanti et al., 2020). The Day plot (Dunlop, 2002, p. 2002) was produced according to M_{rs}/M_s and H_{cr}/H_c to evaluate the grain size for the kamacite-bearing lunar samples based on its implication for the domain state of magnetite-bearing materials (Fig. 2b).

Table 1
Magnetic properties of CE-5 bulk soil CE5C0600 and selected basaltic fragments.

Sample	Mass (mg)	Method	Fe^0	Is/FeO	Parameters
			CE5C0600		
CE5C0600 (Soil)	6.02	VSM	0.42%	14^{+6}_{-10}	M_s: 5.54*10^{-6} Am^2; M_{rs}: 3.70*10^{-7} Am^2 H_c: 5.9 mT; H_{cr}: 16.0 mT
	16.93	EPR			A: 9.31*10^5; ΔH: 860 G Fe^0: 2.5%
	21.15	Mössbauer	0.43%		Pyroxene M1 Fe^{2+} + Olivine Fe^{2+}: 33.4% Pyroxene M2 Fe^{2+} + Glass Fe^{2+}: 55.0% Ilmenite Fe^{2+}: 9.1%
CE5–0600-01	5.18	VSM	0.10%	0	M_s: 1.13*10^{-6} Am^2; M_{rs}: 3.37*10^{-8} Am^2 H_c: 5.2 mT; H_{cr}: 105.8 mT
CE5–0600-02	0.51	EPR			A: 3.29*10^5; ΔH: 868 G
CE5–0600-03	0.42	EPR			A: 2.85*10^5; ΔH: 702 G
CE5–0600-04	0.27	EPR			A: 5.28*10^4; ΔH: 732 G
CE5–0600-05	0.24	EPR			A: 1.19*10^5; ΔH: 640 G
CE5–0600-06	0.17	EPR			A: 1.51*10^5; ΔH: 763 G
			CE5Z0906YJ		
CE5–0906-01	4.88	VSM	0.09%	0	M_s: 1.00*10^{-6} Am^2; M_{rs}: 2.57*10^{-8} Am^2 H_c: 6.9 mT; H_{cr}: 60.8 mT
		EPR			A: 4.43*10^4; ΔH: 748 G
CE5–0906-02	1.57	EPR			A: 2.16*10^4; ΔH: 684 G
CE5–0906-03	0.21	EPR			Weak signal
CE5–0906-04	0.19	EPR			Weak signal
			CE5Z0204YJ		
CE5–0204-01	4.98	VSM	0.08%	0	M_s: 9.10*10^{-7} Am^2; M_{rs}: 1.69*10^{-8} Am^2 H_c: 4.3 mT; H_{cr}: 85.8 mT
		EPR			A: 4.01*10^4; ΔH: 780 G
CE5–0204-02	0.64	EPR			Weak signal
CE5–0204-03	0.34	EPR			Weak signal
CE5–0204-04	0.10	EPR			Weak signal

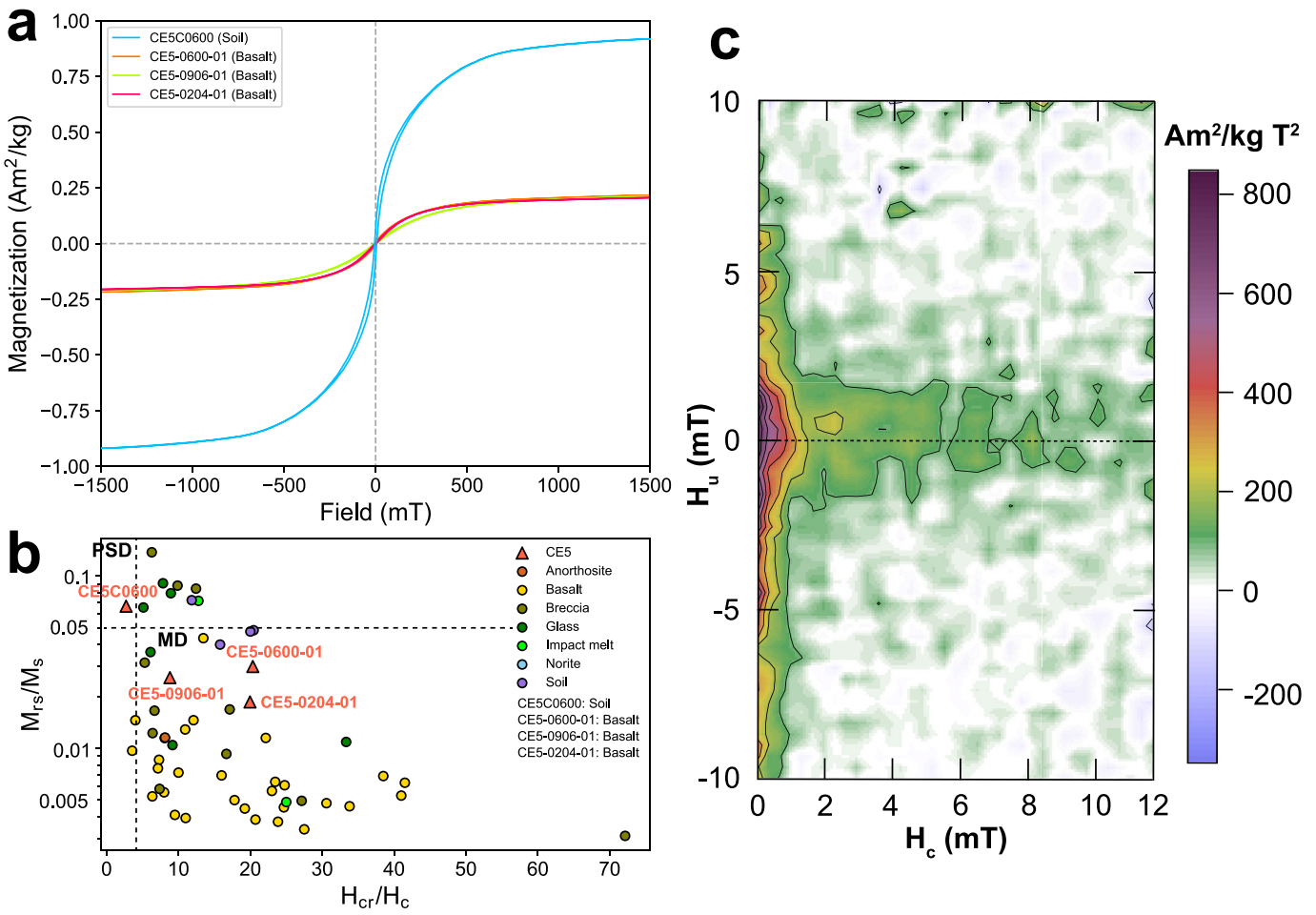

Fig. 2. Vibrating sample magnetometer data of the CE-5 samples. a. Hysteresis loop. b. Day plot of hysteresis parameters. Black dashed lines indicate regions for domain state (PSD, pseudo-single domain; MD, multidomain) of magnetite for reference. c. First-order reversal curve. The vertical and horizontal axes represent H_u (local interaction field) and H_c (coercivity), respectively.

The weight percentage of Fe^0 in the CE-5 lunar soil and lithic fragments was calculated by dividing their M_s values by that of pure metallic iron (218 Am^2/kg) and multiplying by 100, respectively. Besides, M_s values of Apollo samples were measured by VSM in the same way as summarized by Strauss et al. (2021), based on which we did the same calculation to obtain their Fe^0 weight abundance for comparison (Table S1).

In addition, the first-order reversal curves (FORC) diagrams provide much more abundant information about magnetic assemblages than standard hysteresis measurements (Muxworthy and Roberts, 2007), including switching fields and local interaction fields (Roberts et al., 2000). FORCs of the CE-5 lunar soil CE5C0600 were measured by VSM with saturation field of 0.9 T, max H_c field of 12 mT, max H_u field of 10 mT, min H_u field of −10 mT, and averaging time of 0.1 s. The FORC curves were then processed by an Igor program FORCinel v3.08 (Harrison and Feinberg, 2008, p. 200) to derive FORC diagram (Fig. 2c) with a smoothing factor of 8. Superparamagnetic, single-domain, and multidomain grains all have diagnostic manifestations in the FORC diagram (Fig. 10 in Roberts et al., 2000).

2.3. Electron paramagnetic resonance spectrometer

The ferromagnetic resonance (FMR) spectra (Fig. 3a & Fig. S3) of the CE-5 lunar soil CE5C0600 (16.93 mg) and 16 lithic fragments selected from CE5C0600 (CE5-C0600–01 to CE5-C0600–08), CE5Z0906YJ (CE5-0906-01 to CE5-0906-04), and CE5Z0204YJ (CE5-0204-01 to CE5-0204-04), were obtained by the Bruker A300–8/2.7 EPR Spectrometer with a high sensitivity of magnetic field (1 mG) at Badong National Observation and Research Station of Geohazards, China University of Geosciences, Wuhan. The FMR spectra were measured at room temperature operating at a nominal frequency of 9.9 GHz with a sweep width of 10,000 G. Samples were put into a 3.0 mm O.D. - 2.5 mm I.D. quartz tube for measurements. *A* (amplitude of the ferromagnetic resonance) and ΔH (linewidth of the ferromagnetic resonance) values were measured from each obtained FMR spectra.

Typically, Is/FeO (the intensity of the characteristic ferromagnetic resonance normalized to total iron content, where $Is = (\Delta H)^2 A/m$, m represents mass) was calculated directly from the EPR data of Apollo and Luna samples (Morris, 1976). However, since the amplitude is recorded in arbitrary units, that needed to be calibrated by samples with known Is/FeO values. It is not possible for this study to compute them directly from the EPR data; therefore, the FMR spectra were only used for relatively comparison, after normalizing the *A* value of each spectrum to the *A* value of CE5-0906-02 (A_{Norm}).

2.4. Mössbauer spectrometer

The ^{57}Fe Mössbauer spectrum (Fig. 3b) of 21.15 mg CE-5 lunar soil CE5C0600 was recorded by a WSS-10 Mössbauer Spectrometer at the School of Earth Sciences, China University of Geosciences, Wuhan. The spectrum was measured in transmission mode with a 25 mCi ^{57}Co (Rh) source at room temperature for 7 days; the Doppler velocity was calibrated by 25 μm α-Fe. The measured spectrum was then fitted using the Lorentz absorption curve by a commercial software MossWinn4.0

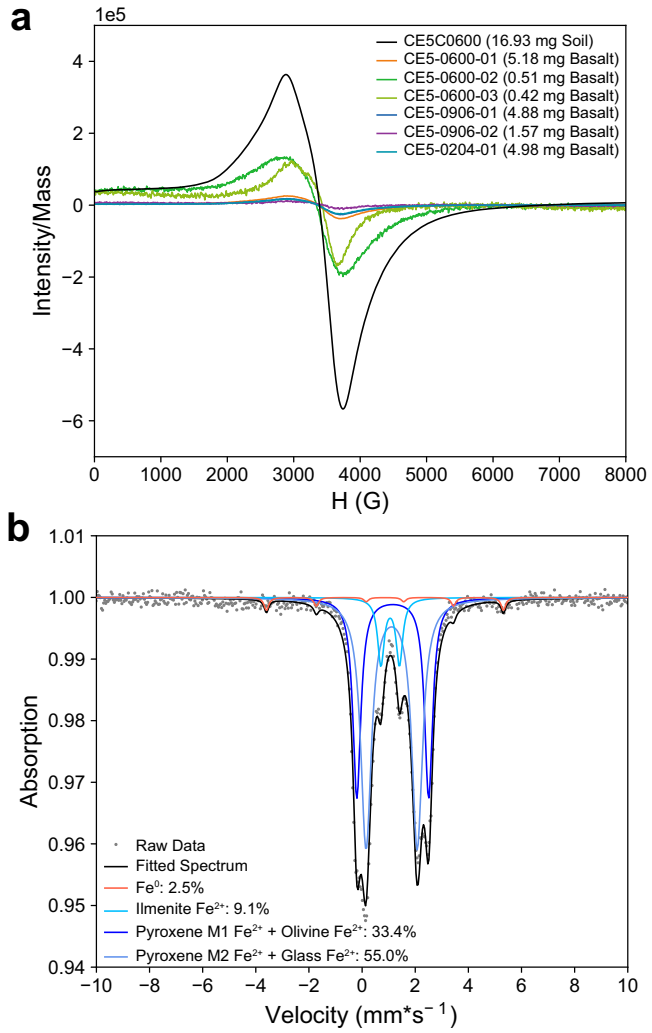

Fig. 3. Ferromagnetic resonance and Mössbauer spectra of the CE-5 samples. a. Ferromagnetic resonance spectra of CE-5 soil and clasts. b. ^{57}Fe Mössbauer spectrum of the CE-5 soil CE5C0600.

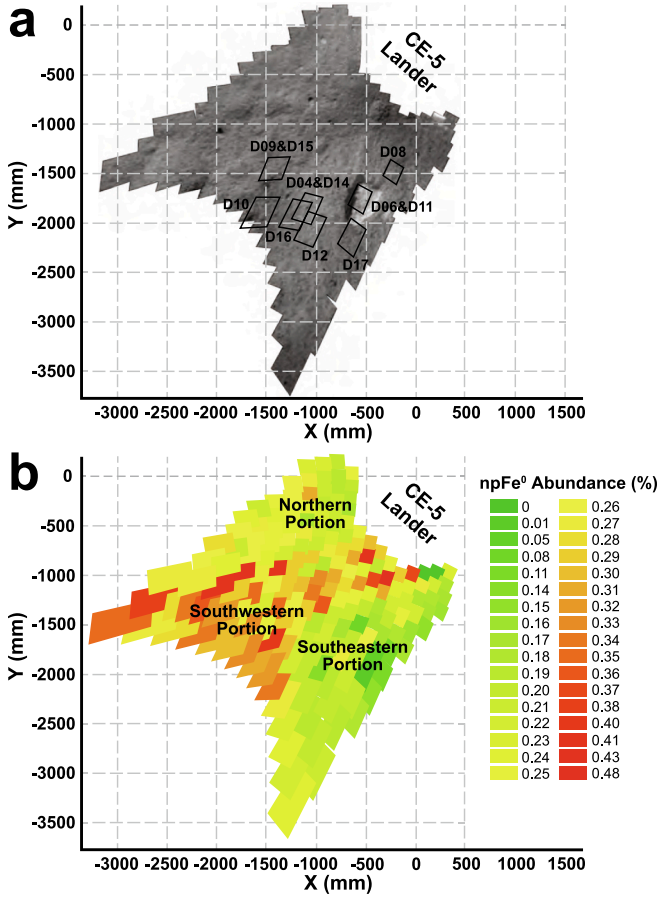

Fig. 4. CE-5 LMS data. a. LMS measurement areas. The black polygons indicate all bands detection mode targets. The basemap is the 900 nm reflectance map acquired in all views scan mode. b. npFe^0 abundance of the CE-5 landing site based on LMS all views scan mode data. North is up.

(http://www.mosswinn.com/english/v4.htm) with a baseline of 2,289,611.512. The relative abundance of Fe^0 (Magnetic 1), the sum of Fe^{2+} in pyroxene M1 site and olivine (Doublet 1), the sum of Fe^{2+} in pyroxene M2 site and glass (Doublet 2), and Fe^{2+} in ilmenite (Doublet 3) was then quantified by integrating the absorption areas of each sub-spectrum. Uncertainties are shown as fitting residuals in Fig. 3b. Mössbauer parameters of these components are presented in Table S2. The Fe^0 abundance in CE5C0600 soil was then calculated on the basis of the relative abundance of Fe^0 in all iron species and the bulk FeO content in the soil.

2.5. Radiative transfer modeling of space weathering products at the landing site

The Lunar Mineralogical Spectrometer (LMS) is an acousto-optic tunable filter spectrometer onboard CE-5 (Xu et al., 2022). LMS has three in-flight operation modes including all bands detection mode, all views scan mode, and calibration mode. In all bands detection mode, LMS obtained spectral images using the VIS channel (480–950 nm) and infrared spectra using three IR channels (NIR, 900–1450 nm; SWIR, 1400–2300 nm; MWIR, 2200–3200 nm) at a sampling interval of 5 nm for 588 bands. In all views scan mode, LMS obtained spectral images using six VIS channels (485, 560, 640, 750, 850, and 900 nm); and infrared spectra in six NIR (950, 1000, 1050, 1100, 1250, and 1450 nm), four SWIR (1550, 1800, 2000, and 2200 nm), and four MWIR channels (2600, 2800, 3000, and 3200 nm), in total of 20 bands.

LMS obtained 11 spectra in all bands detection mode (Fig. 4). 180 images (S001 to S180) and infrared spectra were obtained in all views scan mode, covering an area of 3×3 m^2. We started with Level 2B irradiance data, which underwent dark-current, flat-field, temperature, radiometric, and geometric calibrations (Zhou et al., 2022). The irradiance spectra were then converted to reflectance divided by the solar irradiance (Lin et al., 2020). All LMS scan mode measurements were used for Hapke radiative transfer modeling (Hapke, 2012) to constrain the Fe^0 abundance surrounding the landing site. Our approach is similar to Wang et al. (2017) and Gou et al. (2020): only nanophase iron (npFe^0) abundance was obtained here, mpFe^0 and smFe^0 abundances were not calculated because the Hapke model is not sensitive to them with unknown regolith properties like porosity and compaction. Detailed model descriptions can be found in the supplemental material (Text S1). This model has an accuracy of at least 0.01 wt%, adding 0.001 wt% npFe^0 to lunar soil would cause an apparent change of its reflectance (Gou et al., 2020; Wang et al., 2017).

3. Results

3.1. Magnetic characteristics of the CE-5 soil

According to VSM measurements, the hysteresis loops of CE-5 lunar soil and basaltic fragments are shown in Fig. 2a; on the basis of these data, values of saturation magnetization (M_s), saturation remanent magnetization (M_{rs}), coercivity (H_c), and remanent coercivity (H_{cr}) were

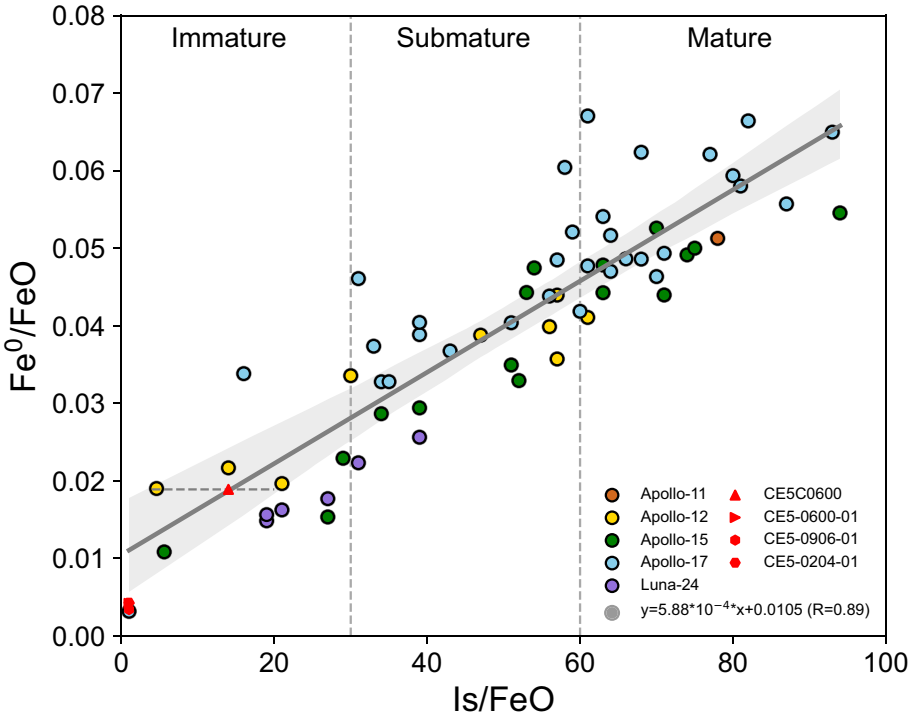

Fig. 5. Relationship between Fe^0/FeO and Is/FeO of lunar mare soils. Data are based on Morris (Morris, 1980) and the current study. The gray area indicates the 99% confidence envelope.

computed by HystLab and HYSITS (see also Section 2.2). The bulk soil CE5C0600 has the highest M_s (5.54×10^{-6} Am^2), followed by three basaltic fragments CE5-0600-01 (1.13×10^{-6} Am^2), CE5-0906-01 (1.00×10^{-6} Am^2), and CE5-0204-01 (9.10×10^{-7} Am^2). Their M_s values yield Fe^0 abundances of 0.42% (CE5C0600), 0.10% (CE5-0600-01), 0.09% (CE5-0906-01), and 0.08% (CE5-0204-01), respectively.

The Is/FeO value is a widely used maturity index (Morris, 1976) but is not possible to compute here based on EPR measurements because of the lack of Apollo samples for calibration (see also Section 2.3). Alternatively, a linear relationship ($y = 5.88 \times 10^{-4}x + 0.0105$) (Fig. 5) between Fe^0/FeO and Is/FeO of lunar mare soils was derived from the data of Morris (1980) (Table S3) using linear regression model. Highland soils were not included because CE-5 samples were collected from a mare unit (Qian et al., 2021b). Based on this linear relationship, the Is/FeO value of the bulk soil CE5C0600 was estimated to be 14^{+6}_{-10} (errors represent 99% confidence interval), considering a Fe^0 abundance of 0.42% and a FeO abundance of 22.22% (obtained by our previous study using the same sample with ICP-MS; Zong et al., 2022). It is among the most immature lunar soils on the Moon (Fig. 5).

The Day plot of hysteresis parameters summarized from the data of Strauss et al. (2021) and the current study (Table S1) is shown in Fig. 2b. Bulk CE5C0600 soil has the highest M_{rs}/M_s and lowest H_{cr}/H_c values compared to the selected clasts, suggesting relatively fine domain state for the bulk soil than the local bedrock basalt and other Apollo soils. CE-5 basaltic fragments (CE5-0600-01, CE5-0906-01, CE5-0204-01) have comparable H_{cr}/H_c values with previous Apollo basalts, but their M_{rs}/M_s values are relatively higher. In addition, the first-order reversal curve (FORC) of bulk soil CE5C0600 has a weak positive peak at around 2 mT and the contours systematically diverge along the Hu axis, forming a triangle distribution in the diagram (Fig. 2c), indicating a pseudo-single domain behavior of the soil.

On the basis of EPR measurements, the FMR spectra of CE-5 soil, and basaltic fragments are shown in Fig. 3a, and those with weak signals are shown in Fig. S3. All obtained FMR spectra of CE5C0600 have diagnostic absorptions of Fe^0 with a g factor of ~2.1. CE-5 bulk soil CE5C0600 has the largest ΔH value (linewidth) for all returned lunar soils (860 G). The FeO abundance and ΔH value of CE5C0600 are located on the linear trend ($y = 15.78 \times x + 494.69$) (Fig. 6a) derived from previous lunar soils (Morris, 1978) (Table S4), indicating the ΔH of CE-5 soil is controlled by composition. The A value (amplitude) of the FMR spectra was used to compare their relative spin concentrations, therefore the relative Fe^0 abundance. The bulk soil CE5C0600 has the largest A value ($43.1 \times A_{Norm}$), followed by CE5-0600-02 ($15.3 \times A_{Norm}$) and CE5-0600-03 ($13.2 \times A_{Norm}$) with glassy coatings on the grain. Other basaltic fragments in the FMR spectra are relatively homogeneous ($3.3 \times A_{Norm}$ in average), as in the hysteresis loops. The bulk soil has a 13 times larger A value than the basaltic fragments, while the bulk soil has 4.7 times larger VSM Fe^0 abundance than the basaltic fragments. This may be due to the fact that VSM and EPR are sensitive to different Fe^0 grain sizes. VSM is sensitive to particles with grain size >2–4 nm (Pearce et al., 1973), and EPR is sensitive to particles with grain size from 4 to 33 nm (Housley et al., 1976). This indicates that the CE-5 bulk soil may be rich in Fe^0 with sizes between 4 and 33 nm, while the basaltic fragments are abundant in Fe^0 > 33 nm from the igneous process, consistent with the Day plot result.

In addition, Mössbauer spectra of CE-5 soil CE5C0600 were obtained (Fig. 3b). It has clear absorptions of pyroxene M1 site Fe^{2+} + olivine Fe^{2+} (33.4%) and M2 site Fe^{2+} + glass Fe^{2+} (55.5%), as well as ilmenite Fe^{2+} site (9.1%). The absorption of Fe^0 is weak, with a relative abundance of 2.5%, corresponding to an absolute abundance of 0.43% in the soil considering its bulk iron composition (Zong et al., 2022). This value matches well with the abundance of the bulk soil (0.42%) measured by

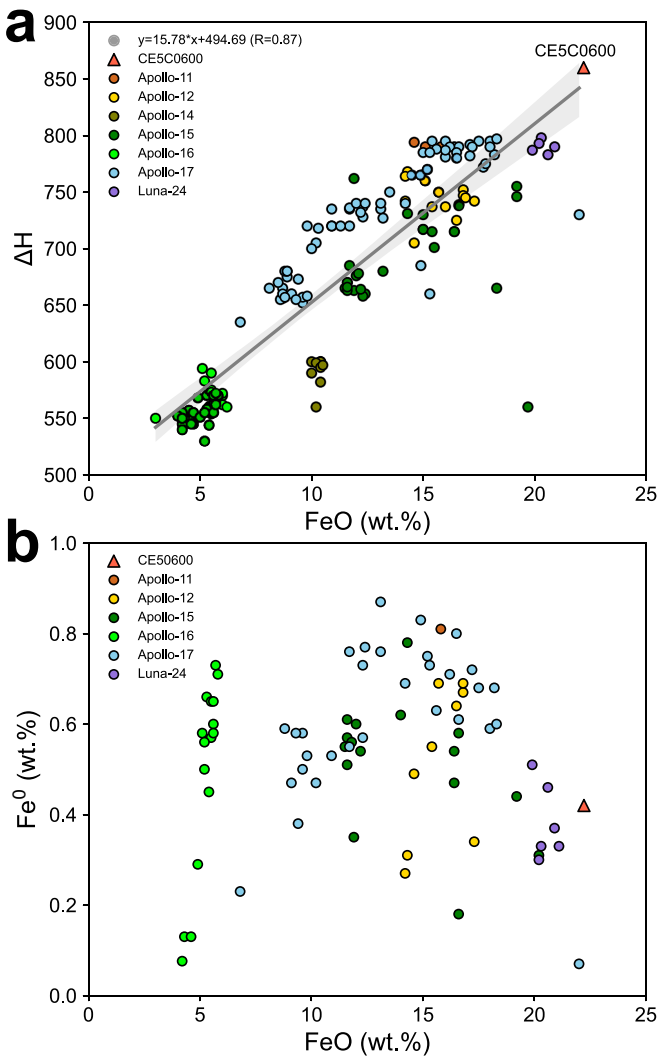

Fig. 6. Relationship between Fe^0, ΔH, and FeO content of lunar soils. a. Relationship between FeO content and ΔH; data are from Morris (1978) and this study. The gray area indicates the 99% confidence envelope. b. Relationship between FeO content and Fe^0; data are from Morris (1980) and this study.

VSM. There is no evidence of Fe^{3+} or other iron species existing in the CE-5 soil, indicating micrometeorite impact-induced disproportionation (Li et al., 2022a; Xian et al., 2023) are rare.

3.2. Nanophase iron abundance at the CE-5 landing site

The $npFe^0$ abundance map (Fig. 4b & Fig. 7a) was produced based on LMS all-views scan mode data (Section 2.5). The area covered by LMS has an average $npFe^0$ abundance of 0.24%, yielding the $mpFe^0$ abundance at the landing site is 0.18% (0.42% determined magnetically – 0.24%). The southwestern portion (~0.3%) of the LMS investigating area has a much higher $npFe^0$ abundance than the southeastern and northern portions (~0.2%) (Fig. 4b & Fig. 7a).

3.3. Rocket exhaust at the CE-5 landing site

The rocket exhaust is a common process altering the surface of a lunar landing site (Clegg et al., 2014). It is widely observed that rocket exhaust of the descent stage alters the landing site soil by blowing away surface materials. The blast zone of Apollo missions is typically ~29,000 km^2 in area and the blast zone of CE-3 lander is ~2530 m^2 (Clegg-Watkins et al., 2016). The CE-5 sampling site is immediately adjacent to the lander, far closer than all Apollo sampling sites to their respective landers, making it more likely to be intensively impacted by rocket exhaust.

The surface soil at the CE-5 landing site was observed to be altered by rocket exhaust. The albedo of the CE-5 site was significantly increased (20%) by the rocket exhaust according to the Lunar Reconnaissance Orbiter Camera Narrow Angle Camera (NAC) images (Robinson et al., 2010) before and after landing (Fig. 1bc), with a blast zone of 691 m^2 and a diameter between 12 and 18 m. The NAC images used were radiometrically calibrated by ISIS3 software (https://isis.astrogeology.usgs.gov/7.0.0/index.html) and stretched in the same way. The lunar blast zone usually consists of a low-reflectance zone (LRZ) in the center, surrounded by a high-reflectance annular zone (HRZ) (Clegg et al., 2014) (their Fig. 1). The HRZ of CE-5 is easily discerned in NAC images, but the LRZ is invisible (Fig. 1c), similar to other uncrewed lunar missions (Clegg et al., 2014). However, we found LRZs could be observed in LCAM images when the CE-5 lander was descending, starting from LCAM 0411 at a nozzle altitude of 13.74 m (Fig. 8). When the lander was approaching the surface, the diameter of the LRZ decreases until it is entirely under the lander, therefore invisible from orbital images (Fig. 1c).

4. Discussion

4.1. Homogeneous origin of the CE-5 lunar basalts

Previous studies investigated the volcanic features in northern Oceanus Procellarum, and suggested that the CE-5 basalts may have erupted from the same source, the vent of Rima Sharp to the north of the landing site in Sinus Roris (Qian et al., 2021a), and underwent similar crystallization process (Chen et al., 2023). It is consistent with the homogeneous composition of the collected basaltic fragments (He et al., 2022; Tian et al., 2021) as well as the magnetic results here. All the investigated basaltic fragments have VSM Fe^0 abundances of ~0.09% with similar EPR *A* values, suggesting the homogeneity of the local basalts.

The relationship between Fe^0 contents of lunar basalts and their FeO contents is shown in Fig. 9 based on the data of Strauss et al. (2021). The Fe^0 contents of CE-5 basalts are intermediate among all lunar basalts and there is no relation between Fe^0 and FeO contents (Fig. 6b) summarized from the data of Morris (1980) and the current study. Fe^0 can also be produced by igneous process as the last product of crystallization (Rochette et al., 2010). The Fe^0 in basalts, with larger domain sizes (Fig. 2b), are more likely related to the igneous process (Morris, 1980, p. 198) rather than space weathering.

4.2. Maturity of the CE-5 lunar soil

Several studies (Li et al., 2021; Lu et al., 2022; Wu et al., 2022) have discussed the maturity of the CE-5 soil (see also Section 1) but they cannot reach an consensus on whether the CE-5 soil is mature or immature, probably because distinct maturity indexes were used.

Is/FeO has been regarded as the gold standard to quantify the maturity state of lunar soils since the Apollo era (Morris, 1978; Morris, 1976). Based on the magnetic measurements here, we suggest the CE-5 soil has an Is/FeO of 14^{+6}_{-10}. It is one of the most immature lunar soils (Fig. 5). Furthermore, we plotted the relationship between agglutinate content (Li et al., 2021), Ni content (Zong et al., 2022), and Is/FeO of CE-5 soil together with previous lunar soils (Fig. 10) summarized from the

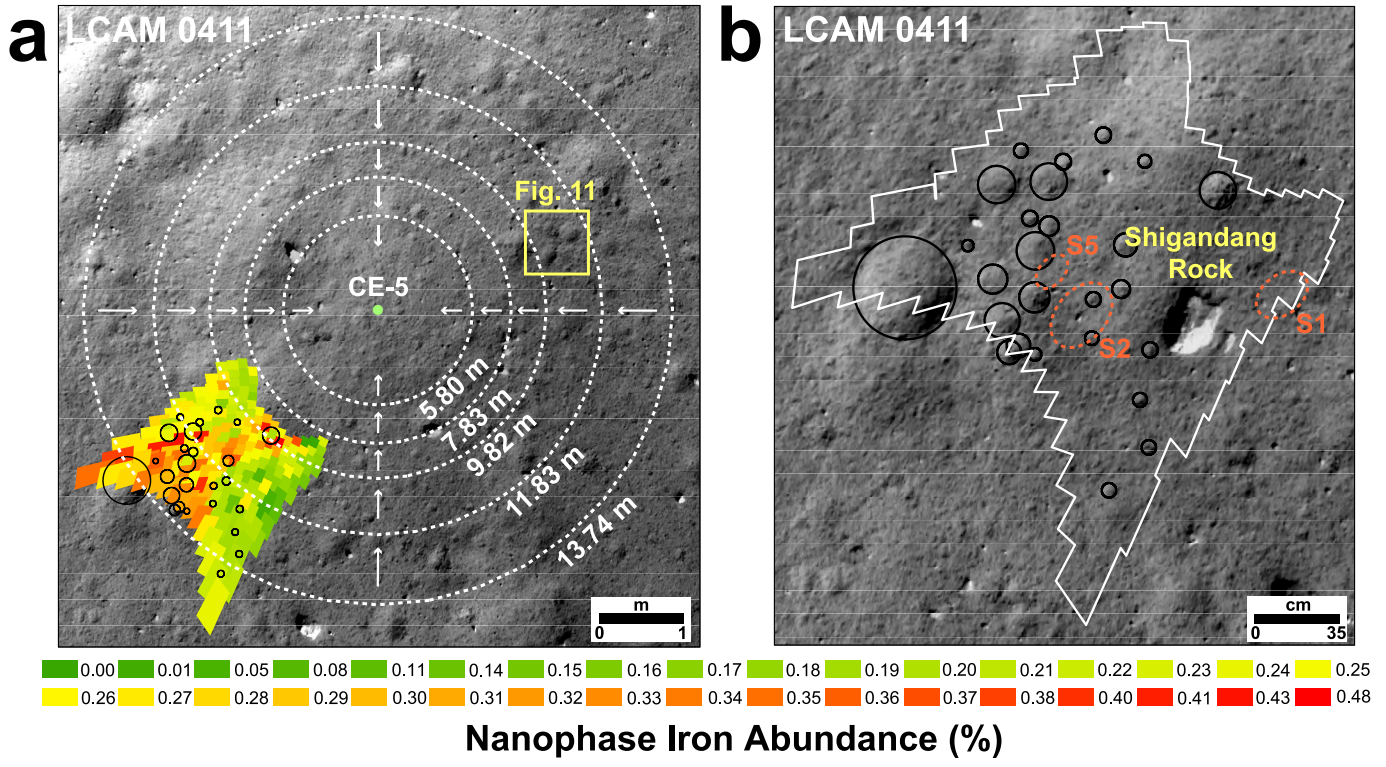

Fig. 7. Lunar Mineralogical Spectrometer investigating area at the CE-5 site. a. LMS $npFe^0$ abundance of the landing site according to the Hapke model. The white dashed circles indicate the low-reflectance zone when the lander descending (white numbers indicate the nozzle altitude). b. Zoomed in view of the LMS investigating area. Centimeter-size impact craters are mainly distributed in the west of the LMS investigating area. S1, S2, and S5 are scoop sampling locations. The basemap is a LCAM image, the white number indicating the image ID. North is up.

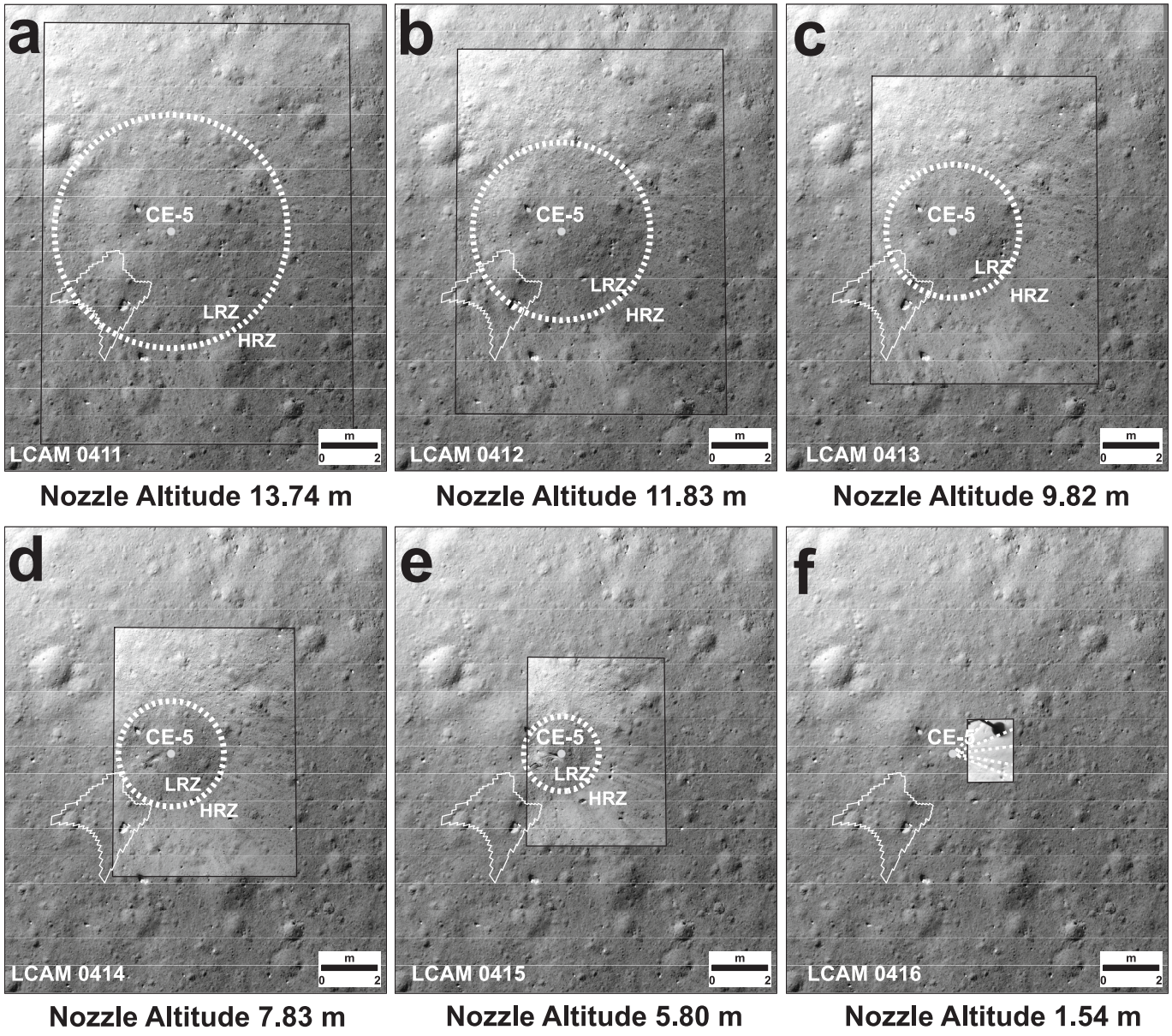

Fig. 8. The relationship between LMS investigating area and the rocket blast zone. LRZ and HRZ represent the low-reflectance and high-reflectance zones, respectively. The thin black rectangles represent the footprints of the LCAM images, the white numbers indicating their IDs. The white dashed circles represent the boundary of LRZ and HRZ. North is up.

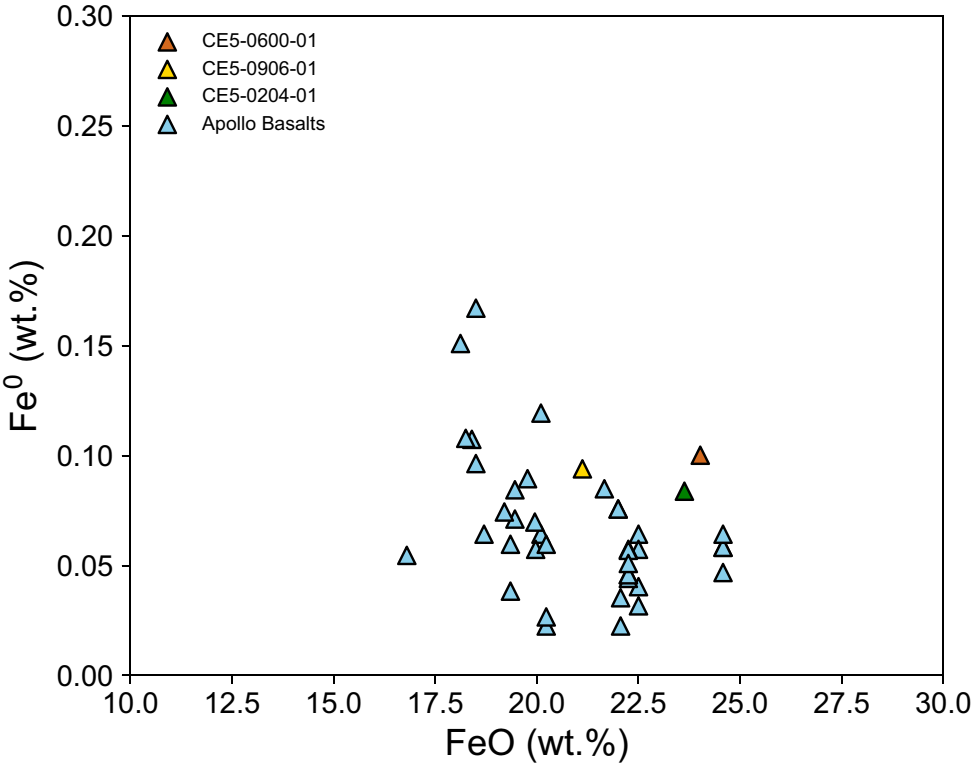

Fig. 9. Relationship between Fe^0 and FeO contents of lunar mare soils. Fe^0 contents are calculated from saturation magnetization from Strauss et al. (2021) and this study. FeO contents are from Lunar Sample Compendium (Meyer, 2012) and this study.

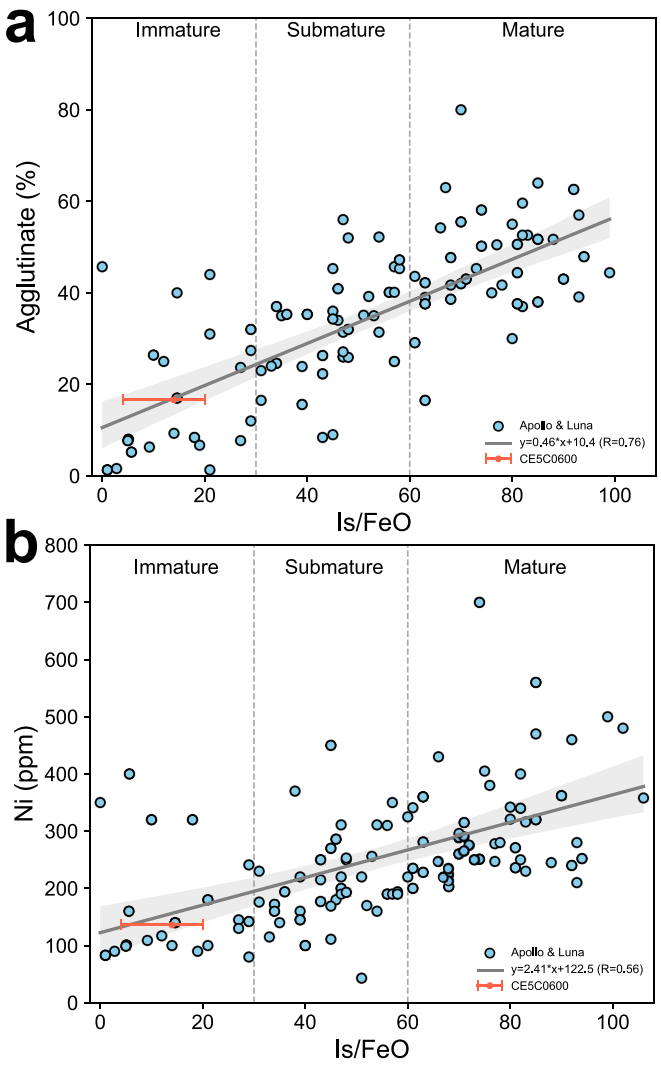

Fig. 10. Relationship between agglutinate content, Ni content, and Is/FeO of lunar soils. a. Relationship between agglutinate content and Is/FeO. b. Relationship between Ni content and Is/FeO. Data are from Graf (1993), the Lunar Sample Compendium (Meyer, 2012), and this study. The gray area indicates the 99% confidence envelope.

data of Graf (1993) and the Lunar Sample Compendium (Meyer, 2012) (Table S5). The point representing CE-5 is located exactly on the linear trend defined by all soils, firmly supporting that the Is/FeO value obtained here is reliable. It can also explain the low agglutinate abundance in the CE-5 soil (~16.6%) (Li et al., 2021), because it is simply immature.

Li et al. (2021) proposed that the CE-5 soil is mature according to its fine grain size. However, inferring the maturity state of a lunar soil based on particle size may not be accurate. The grain size of lunar soil is not only controlled by space weathering but also protolith (Head and Wilson, 2020). It is found that CE-5 basalts experienced fast cooling after eruption (He et al., 2022). Lunar regolith formed on such basalts may be relatively easier to be comminuted with finer crystal size. In addition, the grain size of lunar soil doesn't have a linear trend with maturity, but a competitive relation between micrometeorite comminution and agglutination (McKay et al., 1974). There are little agglutinates in the CE-5 soil, indicating it is in an early evolution stage (Head and Wilson, 2020; McKay et al., 1974) with not enough agglutinate to weld soil grains therefore finer than most of Apollo soils. Besides, compared with the VSM (0.42%) and Mössbauer (0.43%) Fe^0 abundances obtained through more precise magnetic approaches, Lu et al. (2022) significantly overestimated the $smFe^0$ abundance (>1%) and the maturity of the soil. It may be due to the Hapke model is not sensitive to $mpFe^0$ (Wang et al., 2017) or they involved the LMS data with wavelength around 1 μm that have nonnegligible artifacts (Xu et al., 2022).

In summary, on the basis of our analysis of young CE-5 and older Apollo soils, we suggest continuing to use the Is/FeO index as the only diagnostic criterion to distinguish the maturity state of a lunar soil.

4.3. Origin of the immature CE-5 soil

The CE-5 soil is among the most immature lunar soils (Fig. 5). The relatively higher latitude of the sampling site (43.06°N, 51.92°W) compared to all Apollo sites (Fig. 1a), the effects of rocket exhaust, the younger age of the sampling site, or the integrated effects of both may cause its immaturity.

The flux of solar wind tends to decrease toward higher latitude (Kallio et al., 2019), perhaps reducing the maturity of lunar soil. The CE-5 soil may be impacted by latitude because it is higher than all Apollo sites which are close to the equator (Fig. 1a). However, this conjecture is excluded by the returned CE-5 soils. Gu et al. (2022) investigated the microstructures in the CE-5 soil and compared them with those in Apollo soils, suggesting no significant latitude-dependent effects on space weathering. This may be because micrometeorite impact is the main deriver for space weathering and the formation of smFe in the CE-5 soil (Li et al., 2022a; Xian et al., 2023).

The entire CE-5 sampling area is within the rocket blast zone (Fig. 1c & Fig. 7a), with clear evidence of plume-regolith interactions (see also Section 3.3). According to the numerical regolith erosion model, Zhang et al. (2022) proposed the plume of the CE-5 lander eroded the surface within a distance <10 m to the nozzle, by removing ~336 kg of soils, with a maximum erosion depth of ~1 cm. The most fine and mature soils on top were highly likely blown away by the rocket exhaust (Morris, 1978; Wang et al., 2017), that significantly changed the $npFe^0$ abundance of the landing site (Fig. 7a). Besides, the southeastern and northern portions for the $npFe^0$ abundance map of the CE-5 site (Fig. 7a) have lower $npFe^0$ abundance (~0.2%) than the southwestern portion (~0.3%). This asymmetrical distribution is most plausible to be explained by more mature soils having been removed for the southeastern portion with fewer craters (Fig. 7b). Centimeter-sized impact craters are able to be identified according to the CE-5 LCAM images. We found there are more impact craters (25 in total) distributed in the southwestern portion and only one distributed in the southeastern portion (Fig. 7b). Small craters may generate a local turbulent flow in the plume in the southwestern portion due to the concentration of centimeter-sized craters, where the top mature soil is more likely to be persisted or fine soils blown away by the plume closer to the nozzle more easily to be deposited within those craters. It is supported by the observation that two craters next to the lander are darkened (5%) in LCAM images when CE-5 touching down (Fig. 11). In addition, the CE-5 sampling site is located in the HRZ zone (Fig. 8). According to Clegg-Watkins et al. (2016) and You et al. (2021), the LRZ is likely formed by increasing roughness due to the pitting of the soil in the plume stagnation region, and HRZ is formed by the microscopic/macroscopic smoothing of the surface and the removal of the highly mature dark soil by the plume. It may also work at the CE-5 site; we found in the LCAM images, as the lander approaching the surface, the LRZ area becomes rougher (Fig. 12 ab) and the HRZ area becomes smoother and brighter (Fig. 12 cd). Therefore, plume-regolith interactions (Metzger et al., 2011; Watkins et al., 2021) certainly decreased the maturity of the returned CE-5 soils by removing the top mature soil.

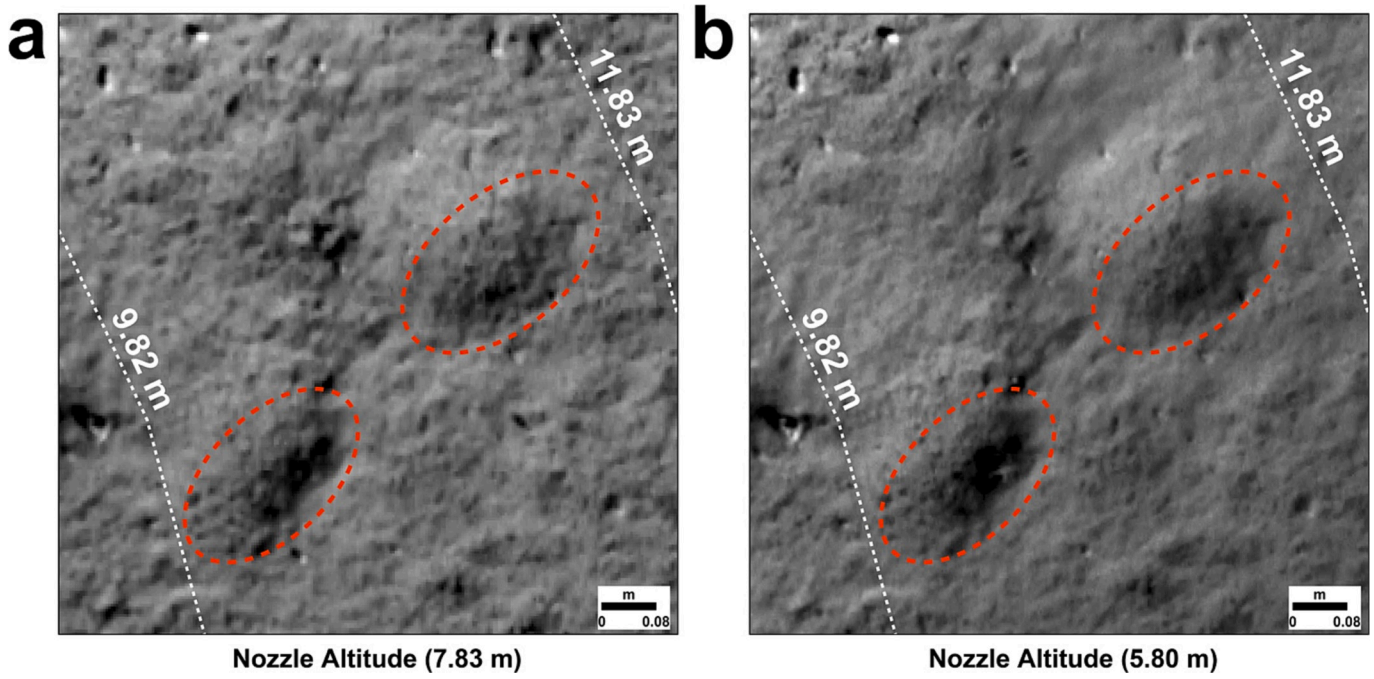

Fig. 11. Rocket exhaust interaction with small impact craters at the CE-5 site. a. LCAM 0414 at a nozzle altitude of 7.83 m. b. LCAM 0415 at a nozzle altitude of 5.80 m. The inner wall of two impact craters delineated by red dashed circles become 5% daker when the lander approaching the surface. (For interpretation of the references to colour in this figure legend, the reader is referred to the web version of this article.)

The young age of the CE-5 landing site may be another cause for the immaturity of the CE-5 soil. CE-5 landed on the Em4 unit (fourth Eratosthenian-aged mare unit in the region) in the northern Oceanus Procellarum (Qian et al., 2021b). The isotopic measurement of basaltic fragments demonstrates that the CE-5 basalts are the youngest ever sampled lunar basalt, with an age of ~2.03 Ga (Che et al., 2021; Li et al., 2021). It is at least 1.0 Ga younger than all Apollo sites (>3.0 Ga) (Snape et al., 2016). The young age likely results in the incomplete growth of lunar soil compared to the older landing sites, with lesser times of overturn, lesser degrees of impact gardening, and a shorter surface residence time for soil grains (Costello et al., 2020; O'Brien and Byrne, 2021). According to the regolith gardening model based on Costello et al. (2020) and a unit age of ~2.0 Ga, only the top ~80 cm of the CE-5 landing site has been gardened. Compared to the Chang'e-4 (CE-4) landing site with an age of ~3.6 Ga (Huang et al., 2018) (~110 cm gardened) similar to the Apollo sites (Snape et al., 2016), the CE-5 site has abundant meter-sized and centimeter-sized boulders but the CE-4 site is smoother with few exposed rocks (Fig. 13). It indicates the CE-4 site is more mature than the CE-5 site because meter-sized boulders can only survive ~150–300 Myr on the lunar surface (Basilevsky et al., 2013). It is consistent with the Is/FeO value of the CE-4 site (82 ± 15; much higher than the CE-5 site) estimated based on *in situ* CE-4 VNIR data (Gou et al., 2020) using similar method to this study (Section 2.5). In addition, the analysis of the CE-5 soil has provided another perspective. Guo et al. (2022a) proposed that the CE-5 soil is in an intermediate stage of space weathering with the occurrence of nanophase wüstite (FeO) by thermal decomposition; this unique microstructure has not been found in any Apollo soils. Only in a more mature stage, wüstite would be reduced into the common Fe^0 (Guo et al., 2022a). Therefore, the young age of the CE-5 site certainly decreased the space weathering degree of the CE-5 soils, compared to Apollo sites.

5. Conclusion

The space weathering of a young mare unit has never been studied because of lacking returned samples until the Chang'e-5 mission to one of the youngest mare units in northern Oceanus Procellarum. In this study, magnetic approaches (Vibrating Sample Magnetometer, Electron Paramagnetic Resonance Spectrometer, and Mössbauer Spectrometer) were used to constrain the space weathering characteristics of the CE-5 soils for the first time with additional information from *in situ* Lunar Mineralogical Spectrometer and Landing Camera observations. Based on the magnetic and spectroscopic constraints at the same time, we found that 1) CE-5 lunar soil is among the most immature lunar soils with a metallic iron abundance of 0.42% and an Is/FeO value of 14^{+6}_{-10}; 2) the metallic iron has a pseudo single domain behavior in the CE-5 soil, may be rich in Fe^0 with size between 4 and 33 nm from space weathering while the basaltic fragments are abundant in Fe^0 > 33 nm from crystallization, 3) CE-5 basaltic fragments are not only homogeneous geochemically but also magnetically indicating a common magmatic origin; 4) Rocket exhaust removed the top more mature lunar soils from the CE-5 landing site, but small-scale craters surrounding the lander may generate a local turbulent plume flow that protects fine soils from removal; 5) The immature nature of the CE-5 soils are the result of young age of the CE-5 landing mare unit and the plume-regolith interactions at the landing site.

It needs to be considered both in engineering and in science that the lunar soils from young units would have a very different maturity state than old landing sites to ensure successful future explorations. The soils from young units may be more immature with abundant rocky fragments that could impede drillings (Su et al., 2022). Rocket exhaust probably disrupts the surface soils that impact returned samples as well as *in situ* investigations especially spectral measurements for surface materials.

CRediT authorship contribution statement

Yuqi Qian: Conceptualization, Methodology, Validation, Investigation, Data curation, Writing – original draft, Writing – review & editing, Visualization. **Long Xiao:** Conceptualization, Writing – original draft, Writing – review & editing, Supervision, Project administration, Funding acquisition. **Jiawei Zhao:** Investigation, Data curation, Writing – original draft, Writing – review & editing. **James W. Head:** Conceptualization, Writing – original draft, Writing – review & editing,

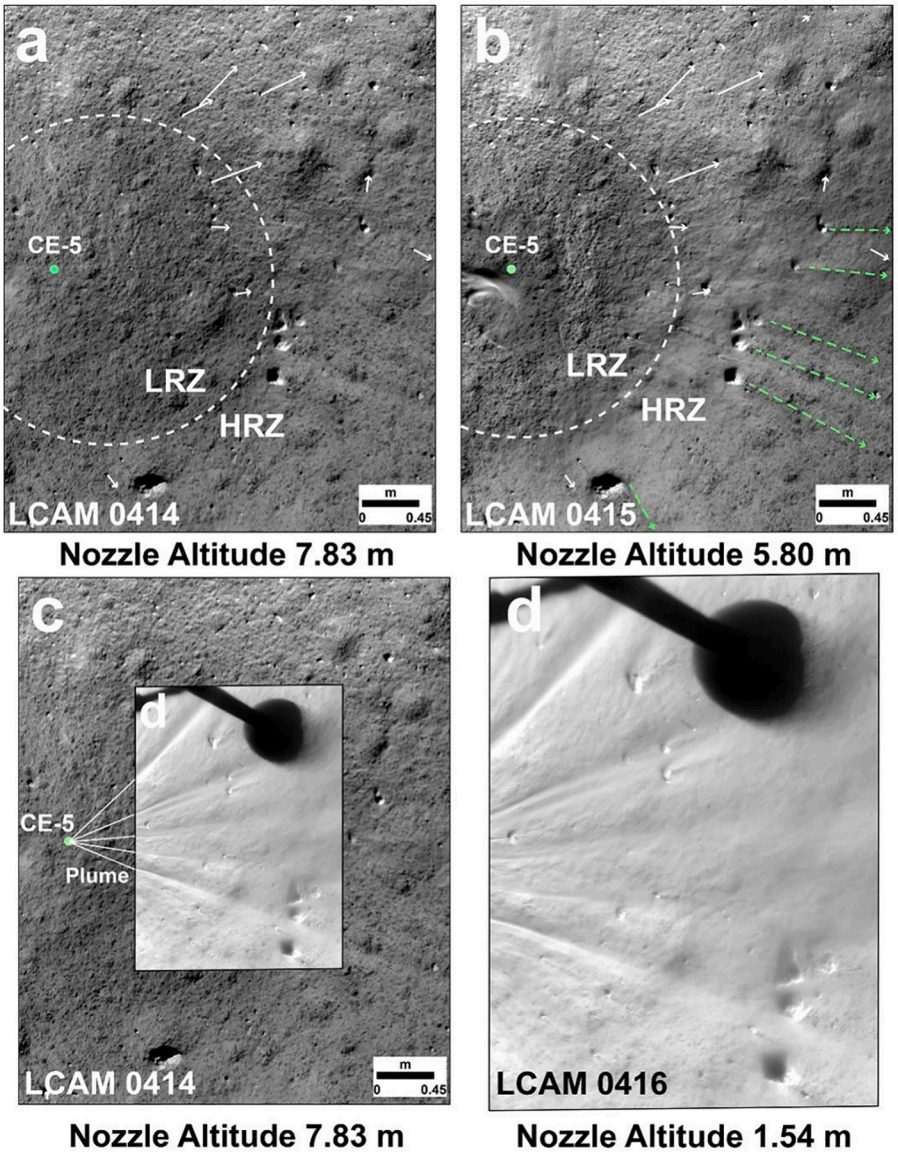

Fig. 12. Rocket exhaust interaction with lunar soil at the CE-5 site. a. b. Centimeter-sized boulders moved by the plume with white arrows indicating the direction. Dark streaks (green arrows) were formed behind large boulders, radial to the nozzle. LRZ becomes rougher when CE-5 descending. c. d. The area of HRZ was significantly smoothed by the plume (white lines). The basemap is LCAM images, the white numbers indicating the image IDs. North is up. (For interpretation of the references to colour in this figure legend, the reader is referred to the web version of this article.)

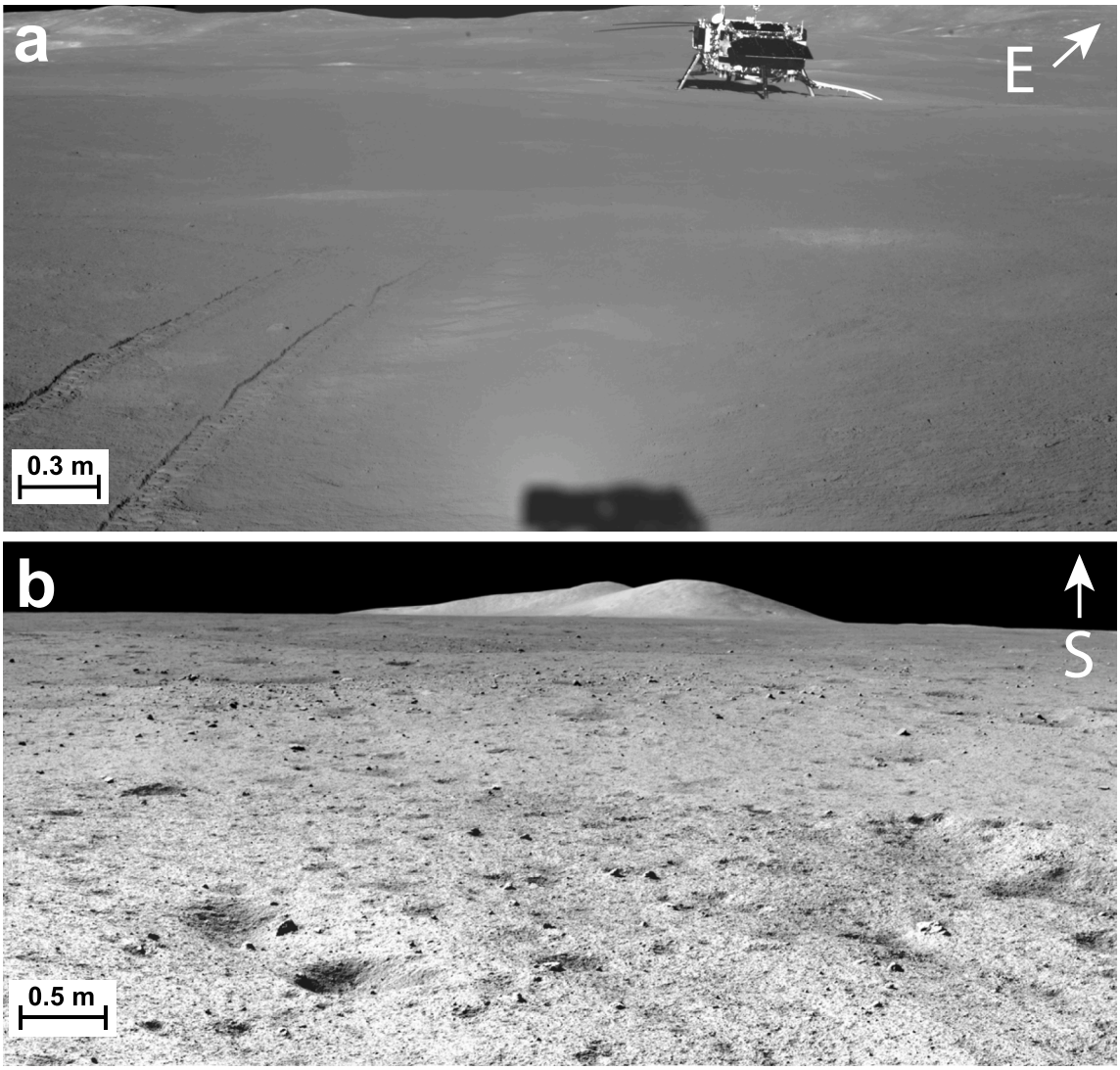

Fig. 13. Panoramic images of the CE-4 and CE-5 landing site. a. CE-4 landing site. b. CE-5 landing site. The CE-4 site is relatively more mature than the CE-5 site with few boulders on the surface. The scale bar only represents for the side close to the camera.

Supervision. **Qi He:** Investigation, Data curation, Writing – original draft, Writing – review & editing. **Huiru Xu:** Investigation, Data curation, Writing – original draft, Writing – review & editing. **Feizhou Wang:** Investigation, Data curation. **Xiaoping Zhang:** Validation, Investigation, Writing – original draft, Writing – review & editing. **Xianquan Ping:** Investigation, Data curation, Writing – original draft, Writing – review & editing. **Wen Zeng:** Investigation, Data curation, Writing – original draft, Writing – review & editing. **Xing Wang:** Validation, Investigation, Writing – original draft, Writing – review & editing. **Joseph Michalski:** Validation, Writing – original draft, Writing – review & editing. **Jiacheng Liu:** Validation, Writing – original draft, Writing – review & editing. **Binlong Ye:** Validation, Writing – original draft, Writing – review & editing. **Meizhu Wang:** Investigation, Data curation. **Lingzhi Sun:** Investigation, Data curation. **Yong Pang:** Investigation, Data curation. **Jiang Wang:** Investigation. **Siyuan Zhao:** Investigation.

Declaration of Competing Interest

The authors declare that they have no known competing financial interests or personal relationships that could have appeared to influence the work reported in this paper.

Data availability

Chang'e-5 samples were applied from China National Space Administration by Long Xiao according to "Notice of China National Space Administration on the Distribution of Procedures for Requesting Lunar Samples". Chang'e-5 LMS data were available from Lunar and Planetary Data Release System (https://moon.bao.ac.cn/web/enmanager/home).

Acknowledgments

We thank the China National Space Administration for providing the Chang'e-5 data and sample. This research is funded by National Key Research and Development Program of China (2020YFE0202100) and the Pre-Research Project on Civil Aerospace Technologies (D020101). We thank the editor, Carol Paty, for handling this paper and the comments from two anonymous reviewers, which have significantly improved this work.

Appendix A. Supplementary data

Supplementary data to this article can be found online at https://doi.org/10.1016/j.icarus.2023.115892.

References

Basilevsky, A.T., Head, J.W., Horz, F., 2013. Survival times of meter-sized boulders on the surface of the Moon. Planet. Space Sci. 89, 118–126. https://doi.org/10.1016/j.pss.2013.07.011.

Bentley, M.S., Ball, A.J., Wright, I.P., Zarnecki, J.C., 2011. On the application of magnetic methods for the characterisation of space weathering products. Planet. Space Sci. 59, 79–91. https://doi.org/10.1016/j.pss.2010.11.008.

Che, X., Nemchin, A., Liu, D., Long, T., Wang, C., Norman, M.D., Joy, K.H., Tartese, R., Head, J., Jolliff, B., Snape, J.F., Neal, C.R., Whitehouse, M.J., Crow, C., Benedix, G., Jourdan, F., Yang, Z., Yang, C., Liu, J., Xie, S., Bao, Z., Fan, R., Li, D., Li, Z., Webb, S. G., 2021. Age and composition of young basalts on the Moon, measured from samples returned by Chang'e-5. Science 374, 887–890. https://doi.org/10.1126/science.abl7957.

Chen, Y., Hu, S., Li, J., Li, Q., Li, Xiongyao, Li, Y., Liu, Y., Qian, Y., Yang, W., Zhou, Q., Lin, Y., Li, C., Li, Xianhua, 2023. Chang'e-5 lunar samples shed new light on the Moon. Innov. Geosci. 1, 100014 https://doi.org/10.59717/j.xinn-geo.2023.100014.

Clegg, R.N., Jolliff, B.L., Robinson, M.S., Hapke, B.W., Plescia, J.B., 2014. Effects of rocket exhaust on lunar soil reflectance properties. Icarus 227, 176–194. https://doi.org/10.1016/j.icarus.2013.09.013.

Clegg-Watkins, R.N., Jolliff, B.L., Boyd, A., Robinson, M.S., Wagner, R., Stopar, J.D., Plescia, J.B., Speyerer, E.J., 2016. Photometric characterization of the Chang'e-3 landing site using LROC NAC images. Icarus 273, 84–95. https://doi.org/10.1016/j.icarus.2015.12.010.

Costello, E.S., Ghent, R.R., Hirabayashi, M., Lucey, P.G., 2020. Impact gardening as a constraint on the age, source, and evolution of ice on Mercury and the Moon. J. Geophys. Res. Planets 125, e2019JE006172. https://doi.org/10.1029/2019JE006172.

Deng, X., Zheng, Y., Jin, S., Yao, M., Zhao, Z., Li, H., Jiang, S., Wang, G., 2021. Design and implementation of sampling, encapsulating, and sealing system of Chang'E-5. Sci. Sin. Technol. 51, 753–762. https://doi.org/10.1360/SST-2021-0093.

Dunlop, D.J., 2002. Theory and application of the Day plot (Mrs/Ms versus Hcr/Hc) 1. Theoretical curves and tests using titanomagnetite data. J. Geophys. Res. Solid Earth 107, EPM 4-1. https://doi.org/10.1029/2001JB000486.

Erdyanti, R.B.T., Antareza, M.A., Tjiongnotoputera, K.D., Mariyanto, M., 2020. HYSITS: a MATLAB code to process vibrating sample magnetometer data (hysteresis loop). J. Phys. Conf. Ser. 1491, 012041 https://doi.org/10.1088/1742-6596/1491/1/012041.

Gou, S., Yue, Z., Di, K., Wan, W., Liu, Z., Liu, B., Peng, M., Wang, Y., He, Z., Xu, R., 2020. In situ spectral measurements of space weathering by Chang'e-4 rover. Earth Planet. Sci. Lett. 535, 116117 https://doi.org/10.1016/j.epsl.2020.116117.

Graf, J.C., 1993. Lunar Soils Grain Size Catalog.

Gu, L., Chen, Y., Xu, Y., Tang, X., Lin, Y., Noguchi, T., Li, J., 2022. Space weathering of the Chang'e-5 lunar sample from a mid-high latitude region on the Moon. Geophys. Res. Lett. 49, e2022GL097875 https://doi.org/10.1029/2022GL097875.

Guo, Z., Li, C., Li, Y., Wen, Y., Wu, Y., Jia, B., Tai, K., Zeng, X., Li, X., Liu, J., Ouyang, Z., 2022a. Sub-microscopic magnetite and metallic iron particles formed by eutectic reaction in Chang'E-5 lunar soil. Nat. Commun. 13, 7177. https://doi.org/10.1038/s41467-022-35009-7.

Guo, J.-G., Ying, T., Gao, H., Chen, Xu, Song, Y., Lin, T., Zhang, Q., Zheng, Q., Li, C., Xu, Y., Chen, Xiaolong, 2022b. Surface microstructures of lunar soil returned by Chang'e-5 mission reveal an intermediate stage in space weathering process. Sci. Bull. 67, 1696–1701. https://doi.org/10.1016/j.scib.2022.06.019.

Hapke, B., 2001. Space weathering from mercury to the asteroid belt. J. Geophys. Res. Planets 106, 10039–10073. https://doi.org/10.1029/2000JE001338.

Hapke, B., 2012. Theory of Reflectance and Emittance Spectroscopy, 2nd ed. Cambridge University Press, Cambridge. https://doi.org/10.1017/CBO9781139025683.

Harrison, R.J., Feinberg, J.M., 2008. FORCinel: an improved algorithm for calculating first-order reversal curve distributions using locally weighted regression smoothing. Geochem. Geophys. Geosyst. 9 https://doi.org/10.1029/2008GC001987.

He, Q., Li, Y., Baziotis, I., Qian, Y., Xiao, L., Wang, Z., Zhang, W., Luo, B., Neal, C.R., Day, J.M.D., Pan, F., She, Z., Wu, X., Hu, Z., Zong, K., Wang, L., 2022. Detailed petrogenesis of the unsampled Oceanus Procellarum: the case of the Chang'e-5 mare basalts. Icarus 383, 115082. https://doi.org/10.1016/j.icarus.2022.115082.

Head, J.W., Wilson, L., 2020. Rethinking lunar Mare basalt regolith formation: new concepts of lava flow Protolith and evolution of regolith thickness and internal structure. Geophys. Res. Lett. 47, e2020GL088334 https://doi.org/10.1029/2020GL088334.

Housley, R.M., Cirlin, E.H., Goldberg, I.B., Crowe, H., 1976. Ferromagnetic resonance studies of lunar core stratigraphy. In: Presented at the 7th Lunar Science Conference, pp. 13–26.

Huang, J., Xiao, Z., Flahaut, J., Martinot, M., Head, J., Xiao, X., Xie, M., Xiao, L., 2018. Geological characteristics of Von Kármán crater, Northwestern South Pole-Aitken Basin: Chang'E-4 landing site region. J. Geophys. Res. Planets 123, 1684–1700. https://doi.org/10.1029/2018JE005577.

Kallio, E., Dyadechkin, S., Wurz, P., Khodachenko, M., 2019. Space weathering on the Moon: Farside-nearside solar wind precipitation asymmetry. Planet. Space Sci. 166, 9–22. https://doi.org/10.1016/j.pss.2018.07.013.

Keller, L.P., McKay, D.S., 1997. The nature and origin of rims on lunar soil grains. Geochim. Cosmochim. Acta 61, 2331–2341. https://doi.org/10.1016/S0016-7037(97)00085-9.

Li, Q.-L., Zhou, Q., Liu, Y., Xiao, Z., Lin, Y., Li, J.-H., Ma, H.-X., Tang, G.-Q., Guo, S., Tang, X., Yuan, J.-Y., Li, J., Wu, F.-Y., Ouyang, Z., Li, C., Li, X.-H., 2021. Two-billion-year-old volcanism on the Moon from Chang'e-5 basalts. Nature 600, 54–58. https://doi.org/10.1038/s41586-021-04100-2.

Li, Chen, Guo, Z., Li, Y., Tai, K., Wei, K., Li, X., Liu, J., Ma, W., 2022a. Impact-driven disproportionation origin of nanophase iron particles in Chang'e-5 lunar soil sample. Nat. Astron. https://doi.org/10.1038/s41550-022-01763-3.

Li, Chunlai, Hu, H., Yang, M.-F., Pei, Z.-Y., Zhou, Q., Ren, X., Liu, B., Liu, D., Zeng, X., Zhang, G., Zhang, H., Liu, J., Wang, Q., Deng, X., Xiao, C., Yao, Y., Xue, D., Zuo, W., Su, Y., Wen, W., Ouyang, Z., 2022b. Characteristics of the lunar samples returned by the Chang'E-5 mission. Natl. Sci. Rev. 9, nwab188 https://doi.org/10.1093/nsr/nwab188.

Lin, Honglei, He, Z., Yang, W., Lin, Y., Xu, R., Zhang, C., Zhu, M.-H., Chang, R., Zhang, J., Li, C., Lin, Hongyu, Liu, Y., Gou, S., Wei, Y., Hu, S., Xue, C., Yang, J., Zhong, J., Fu, X., Wan, W., Zou, Y., 2020. Olivine-norite rock detected by the lunar rover Yutu-2 likely crystallized from the SPA-impact melt pool. Natl. Sci. Rev. 7, 913–920. https://doi.org/10.1093/nsr/nwz183.

Lu, X., Chen, J., Ling, Z., Liu, C., Fu, X., Qiao, L., Zhang, J., Cao, H., Liu, J., He, Z., Xu, R., 2022. Mature lunar soils from Fe-rich and young mare basalts in the Chang'e-5 regolith samples. Nat. Astron. https://doi.org/10.1038/s41550-022-01838-1.

McKay, D.S., Fruland, R.M., Heiken, G.H., 1974. Grain size and the evolution of lunar soils. In: 5th Lunar Science Conference. Presented at the 5th Lunar Science Conference, pp. 887–906.

Metzger, P.T., Smith, J., Lane, J.E., 2011. Phenomenology of soil erosion due to rocket exhaust on the Moon and the Mauna Kea lunar test site. J. Geophys. Res. Planets 116. https://doi.org/10.1029/2010JE003745.

Meyer, C., 2012. Lunar Sample Compendium [WWW Document]. URL. https://curator.jsc.nasa.gov/lunar/lsc/index.cfm.

Morris, R.V., 1976. Surface exposure indices of lunar soils: a comparative FMR study. In: 7th Lunar Science Conference, pp. 315–335.

Morris, R.V., 1978. The surface exposure (maturity) of lunar soils: Some concepts and Is/FeO compilation. In: 9th Lunar and Planetary Science Conference. Lunar and Planetary Institute, Houston, Texas, pp. 2287–2297.

Morris, R.V., 1980. Origins and size distribution of metallic Iron in the lunar regolith. In: 11th Lunar and Planetary Science Conference. Lunar and Planetary Institute, Houston, Texas, pp. 1697–1712.

Morris, R.V., Klingelhöfer, G., Korotev, R.L., Shelfer, T.D., 1998. Mössbauer mineralogy on the Moon: the lunar regolith. Hyperfine Interact. 117, 405–432. https://doi.org/10.1023/A:1012699511670.

Muxworthy, A.R., Roberts, A.P., 2007. First-order reversal curve (FORC) diagrams. In: Gubbins, D., Herrero-Bervera, E. (Eds.), Encyclopedia of Geomagnetism and Paleomagnetism. Springer, Netherlands, Dordrecht, pp. 266–272. https://doi.org/10.1007/978-1-4020-4423-6_99.

Noble, S.K., Pieters, C.M., Keller, L.P., 2007. An experimental approach to understanding the optical effects of space weathering. Icarus 192, 629–642. https://doi.org/10.1016/j.icarus.2007.07.021.

O'Brien, P., Byrne, S., 2021. Physical and chemical evolution of lunar Mare regolith. J. Geophys. Res. Planets 126, e2020JE006634. https://doi.org/10.1029/2020JE006634.

Paterson, G.A., Zhao, X., Jackson, M., Heslop, D., 2018. Measuring, processing, and analyzing hysteresis data. Geochem. Geophys. Geosyst. 19, 1925–1945. https://doi.org/10.1029/2018GC007620.

Pearce, G.W., Gose, W.A., Strangway, D.W., 1973. Magnetic studies on Apollo 15 and 16 lunar samples. In: 4th Lunar Science Conference, pp. 3045–3076.

Pieters, C.M., Noble, S.K., 2016. Space weathering on airless bodies. J. Geophys. Res. Planets 121, 1865–1884. https://doi.org/10.1002/2016JE005128.

Qian, Y., Xiao, L., Head, J.W., Wilson, L., 2021a. The Long sinuous Rille system in northern Oceanus Procellarum and its relation to the Chang'e-5 returned samples. Geophys. Res. Lett. 48, e2021GL092663 https://doi.org/10.1029/2021GL092663.

Qian, Y., Xiao, L., Wang, Q., Head, J.W., Yang, R., Kang, Y., van der Bogert, C.H., Hiesinger, H., Lai, X., Wang, G., Pang, Y., Zhang, N., Yuan, Y., He, Q., Huang, J., Zhao, J., Wang, J., Zhao, S., 2021b. China's Chang'e-5 landing site: geology, stratigraphy, and provenance of materials. Earth Planet. Sci. Lett. 561, 116855 https://doi.org/10.1016/j.epsl.2021.116855.

Roberts, A.P., Pike, C.R., Verosub, K.L., 2000. First-order reversal curve diagrams: a new tool for characterizing the magnetic properties of natural samples. J. Geophys. Res. Solid Earth 105, 28461–28475. https://doi.org/10.1029/2000JB900326.

Robinson, M.S., Brylow, S.M., Tschimmel, M., Humm, D., Lawrence, S.J., Thomas, P.C., Denevi, B.W., Bowman-Cisneros, E., Zerr, J., Ravine, M.A., Caplinger, M.A., Ghaemi, F.T., Schaffner, J.A., Malin, M.C., Mahanti, P., Bartels, A., Anderson, J., Tran, T.N., Eliason, E.M., McEwen, A.S., Turtle, E., Jolliff, B.L., Hiesinger, H., 2010. Lunar Reconnaissance Orbiter Camera (LROC) instrument overview. Space Sci. Rev. 150, 81–124. https://doi.org/10.1007/s11214-010-9634-2.

Rochette, P., Gattacceca, J., Ivanov, A.V., Nazarov, M.A., Bezaeva, N.S., 2010. Magnetic properties of lunar materials: meteorites, Luna and Apollo returned samples. Earth Planet. Sci. Lett. 292, 383–391. https://doi.org/10.1016/j.epsl.2010.02.007.

Snape, J.F., Nemchin, A.A., Bellucci, J.J., Whitehouse, M.J., Tartèse, R., Barnes, J.J., Anand, M., Crawford, I.A., Joy, K.H., 2016. Lunar basalt chronology, mantle differentiation and implications for determining the age of the Moon. Earth Planet. Sci. Lett. 451, 149–158. https://doi.org/10.1016/j.epsl.2016.07.026.

Strauss, B.E., Tikoo, S.M., Gross, J., Setera, J.B., Turrin, B., 2021. Constraining the decline of the lunar dynamo field at ≈3.1 Ga through Paleomagnetic analyses of Apollo 12 Mare basalts. J. Geophys. Res. Planets 126, e2020JE006715. https://doi.org/10.1029/2020JE006715.

Su, Y., Wang, R., Deng, X., Zhang, Z., Zhou, J., Xiao, Z., Ding, C., Li, Y., Dai, S., Ren, X., Zeng, X., Gao, X., Liu, J., Liu, D., Liu, B., Zhou, B., Fang, G., Li, C., 2022. Hyperfine structure of regolith unveiled by Chang'E-5 lunar penetrating radar. IEEE Trans. Geosci. Remote Sens. 1 https://doi.org/10.1109/TGRS.2022.3148200.

Thompson, M.S., Zega, T.J., Becerra, P., Keane, J.T., Byrne, S., 2016. The oxidation state of nanophase Fe particles in lunar soil: implications for space weathering. Meteorit. Planet. Sci. 51, 1082–1095. https://doi.org/10.1111/maps.12646.

Tian, H.-C., Wang, H., Chen, Y., Yang, W., Zhou, Q., Zhang, C., Lin, H.-L., Huang, C., Wu, S.-T., Jia, L.-H., Xu, L., Zhang, D., Li, X.-G., Chang, R., Yang, Y.-H., Xie, L.-W., Zhang, D.-P., Zhang, G.-L., Yang, S.-H., Wu, F.-Y., 2021. Non-KREEP origin for Chang'e-5 basalts in the Procellarum KREEP terrane. Nature 600, 59–63. https://doi.org/10.1038/s41586-021-04119-5.

Wang, Z., Wu, Y., Blewett, D.T., Cloutis, E.A., Zheng, Y., Chen, J., 2017. Submicroscopic metallic iron in lunar soils estimated from the in situ spectra of the Chang'E-3 mission. Geophys. Res. Lett. 44, 3485–3492. https://doi.org/10.1002/2017GL072652.

Watkins, R.N., Metzger, P.T., Mehta, M., Han, D., Prem, P., Sibille, L., Dove, A., Jolliff, B., Moriarty, D.P., Barker, D.C., Patrick, E., Kuhns, M., Laine, M., Radley, C.F., 2021. Understanding and mitigating plume effects during powered descents on the Moon and Mars. Bull. AAS 53. https://doi.org/10.3847/25c2cfeb.f9243994.

Wu, X., Liu, Y., Yang, Y., Guo, D., Du, J., Li, S., Lin, H., Fu, X., Xiao, Z., Xu, Y., Xu, R., He, Z., Zhang, F., Lin, Y., Zou, Y., 2022. Mineralogy and regolith maturity at the Chang'E-5 landing site inferred from the lunar mineralogical spectrometer. Earth Planet. Sci. Lett. 594, 117747 https://doi.org/10.1016/j.epsl.2022.117747.

Xian, H., Zhu, J., Yang, Y., Li, S., Lin, X., Xi, J., Xing, J., Wu, X., Yang, H., Zhou, Q., Tsuchiyama, A., He, H., Xu, Y.-G., 2023. Ubiquitous and progressively increasing ferric iron content on the lunar surfaces revealed by the Chang'e-5 sample. Nat. Astron. https://doi.org/10.1038/s41550-022-01855-0.

Xu, R., Li, C., Yuan, L., Lv, G., Xu, S., Li, F., Jin, J., Wang, Z., Pan, W., Wang, R., Wang, M., Xie, J., Yang, J., Wang, J., He, Z., 2022. Lunar mineralogical spectrometer on Chang'E-5 Mission. Space Sci. Rev. 218, 41. https://doi.org/10.1007/s11214-022-00910-6.

You, J., Zhang, X., Zhang, Haiyan, Li, C., Xu, Yi, Yan, Q., Yu, H., Liu, J., Li, Y., Wang, Yi, Zhao, C., Zhang, He, Xu, Yingqiao, Chen, L., Lin, H., Fu, Q., Gao, Y., Wang, Yuming, Wang, W., Zhi, Q., 2021. Analysis of plume–lunar surface interaction and soil erosion during the Chang'E-4 landing process. Acta Astronaut. 185, 337–351. https://doi.org/10.1016/j.actaastro.2021.05.009.

Zhang, H., Li, C., You, J., Zhang, X., Wang, Yi, Chen, L., Fu, Q., Zhang, B., Wang, Yuming, 2022. The investigation of plume-regolith interaction and dust dispersal during Chang'E-5 descent stage. Aerospace 9. https://doi.org/10.3390/aerospace9070358.

Zheng, Y., Yang, M., Deng, X., Jin, S., Peng, J., Su, Y., Gu, Z., Chen, L., Pang, Y., Zhang, N., 2022. Analysis of Chang'e-5 lunar core drilling process. Chin. J. Aeronaut. https://doi.org/10.1016/j.cja.2022.01.023.

Zhou, C., Jia, Y., Liu, J., Li, H., Fan, Y., Zhang, Z., Liu, Y., Jiang, Y., Zhou, B., He, Z., Yang, J., Hu, Y., Liu, Z., Qin, L., Lv, B., Fu, Z., Yan, J., Wang, C., Zou, Y., 2022. Scientific objectives and payloads of the lunar sample return mission—Chang'e-5. Adv. Space Res. 69, 823–836. https://doi.org/10.1016/j.asr.2021.09.001.

Zong, K., Wang, Z., Li, J., He, Q., Li, Y., Becker, H., Zhang, W., Hu, Z., He, T., Cao, K., She, Z., Wu, X., Xiao, L., Liu, Y., 2022. Bulk compositions of the Chang'e-5 lunar soil: insights into chemical homogeneity, exotic addition, and origin of landing site basalts. Geochim. Cosmochim. Acta. https://doi.org/10.1016/j.gca.2022.06.037.